INTERFACE

royalsocietypublishing.org/journal/rsif

Research



Cite this article: Yuk J, Chakraborty A, Cheng S, Chung C-I, Jorgensen A, Basu S, Chamorro LP, Jung S. 2022 On the design of particle filters inspired by animal noses. *J. R. Soc. Interface* **19**: 20210849. https://doi.org/10.1098/rsif.2021.0849

Received: 4 November 2021 Accepted: 3 February 2022

Subject Category:

Life Sciences-Engineering interface

Subject Areas:

biometrics, biomechanics

Keywords:

passive filter, particle capture, animal nose

Authors for correspondence:

Saikat Basu

e-mail: Saikat.Basu@sdstate.edu

Leonardo P. Chamorro

e-mail: lpchamo@illinois.edu

Sunghwan Jung

e-mail: sunnyjsh@cornell.edu

Electronic supplementary material is available online at https://doi.org/10.6084/m9.figshare. c.5859630.

THE ROYAL SOCIETY

On the design of particle filters inspired by animal noses

Jisoo Yuk¹, Aneek Chakraborty², Shyuan Cheng³, Chun-I Chung³, Ashley Jorgensen⁴, Saikat Basu⁴, Leonardo P. Chamorro³ and Sunghwan Jung¹

SJ, 0000-0002-1420-7921

Passive filtering is a common strategy to reduce airborne disease transmission and particulate contaminants across scales spanning orders of magnitude. The engineering of high-performance filters with relatively low flow resistance but high virus- or particle-blocking efficiency is a non-trivial problem of paramount relevance, as evidenced in the variety of industrial filtration systems and face masks. Next-generation industrial filters and masks should retain sufficiently small droplets and aerosols while having low resistance. We introduce a novel 3D-printable particle filter inspired by animals' complex nasal anatomy. Unlike standard randommedia-based filters, the proposed concept relies on equally spaced channels with tortuous airflow paths. These two strategies induce distinct effects: a reduced resistance and a high likelihood of particle trapping by altering their trajectories with tortuous paths and induced local flow instability. The structures are tested for pressure drop and particle filtering efficiency over different airflow rates. We have also cross-validated the observed efficiency through numerical simulations. We found that the designed filters exhibit a lower pressure drop, compared to commercial masks and filters, while capturing particles bigger than approximately 10 μm. Our findings could facilitate a novel and scalable filter concept inspired by animal noses.

1. Introduction

The control of airborne disease transmission and contaminants has been of central priority across various scientific and engineering disciplines in the last decades. Despite the technological advancements, the emergence of new material designs [1] and a better understanding of the particle-capture processes, passive filtering remains a widely used method to address multiple needs across scales and operational requirements. Most standard filters on the market rely on porous membranes and fibrous structures [2,3]. However, high filtration efficiency requires sufficiently small pores and holes, which may induce excessive pressure drop and, eventually, clogging [3]. Fibre-based filters consist of random arrangements of fibre networks of different composition [4], where interception, inertial impact, diffusion and gravitational settling [5] are the main mechanisms to capture particles.

Physical experiments, numerical simulations and mathematical modelling [6,7] have been extensively used to characterize the filtration efficiency, which provide new insight into an optimal design and underlying working principles. Analysis of pores in a statistically homogeneous, isotropic or anisotropic grid of fibres by Castro & Ostoja-Starzewski [8] and Bliss *et al.* [9] showed that the probability of particulate retention approaches unity only in the limit of infinitely dense systems. They pointed out that there are always comparatively large pores where particles can percolate in any randomly structured filters.

¹Department of Biological and Environmental Engineering, Cornell University, Ithaca, NY 14850, USA

²Department of Mechanical Engineering, Jadavpur University, Kolkata, West Bengal 700032, India ³Department of Mechanical Science and Engineering, University of Illinois at Urbana-Champaign, Urbana, IL 61820, USA

⁴Department of Mechanical Engineering, South Dakota State University, Brookings, SD 57007, USA

royalsocietypublishing.org/journal/rsif J. R. Soc. Interface 19: 20210849

Fibre-based filters are ubiquitous in heating, ventilation, air conditioning (HVAC) systems, industrial processes and personal respirators. Both solid and liquid aerosols, which are primary targets in designing such filters, can severely impact human health. For instance, particulate matters of sizes smaller than 2.5 µm can reach the thoracic region and the circulatory system and cause respiratory and cardiovascular diseases [10]. In particular, droplets (typically $\gtrsim 5 \,\mu m$) and aerosols (≤5 µm) generated via coughing, sneezing and speech have been shown to transport various pathogens [11-13]. While the hazardous size range for inhaled droplets and aerosols that may trigger the initial infection hot-spot along the upper airway is roughly 2-20 µm [14], data from the same study suggest that more than 80% of the viral load responsible for launching upper respiratory tract infections is carried by inhaled droplets with diameters greater than 9 µm; here we have focused on testing the filtration parameters for such particle sizes. Note that although increasing a filter's particle-capture efficiency could be modulated by, e.g. smaller inlet holes and multiple layers of fibres, the process is still at the expense of higher power requirements to drive air transport. Capturing efficiency and associated pressure drop are central factors in designing a filter [15]. The latter is linearly related to velocity in Stokes flows and exhibits a quadratic relationship at sufficiently high Reynolds numbers.

Animals are known to have a much better sense of smell than humans; e.g. approximately 50 times for mice, 200 times for dogs and 700 times for pigs [16]. Most of those with highly evolved olfactory systems have tortuous air pathways along the nasal cavity with long and curved turbinates that split and stretch the inhaled air's streamlines. The multiscale morphological structures and other biological features help capture tiny particles from the inhaled air onto the olfactory epithelium [17,18]. Airpath twists induce secondary flows, including the so-called Dean's pattern. Such motions increase the residence time of particles travelling into the nose system and the likelihood of capture, resulting in highly efficient filtering.

Inspired by this biological mechanism, we have developed three-dimensional (3D)-printable filters that employ distinct features of animals' nasal structures. Our passive filter concept comprises a parallel array of conduits with organized, simplified tortuosity set by analysing the characteristic dimensions of animals' nasal cavities through computed tomography (CT) scan images. The pressure drop and particle filtering efficiency of the proposed concept are measured through experiments and simulations and are compared with their commercial counterparts. It is also worth pointing out that fibre-based commercial filters may change filtration efficiency and pressure drop when exposed to solid–liquid and liquid–solid aerosols [19]; however, the performance of the proposed concept is agnostic to the constitution of particulates and droplets.

2. Results

2.1. Animal nasal cavity analysis

We first characterized the nasal cavity structure of nine distinct mammal species (see Methods). Figure 1*a*,*b* illustrates cross-sectional views of nasal cavities of selected adult mammals. These images are anatomical or CT-scanned photos in a

plane perpendicular to a line connecting the nostril and the nasopharynx, i.e. coronal view. Many animals have very thin and elongated turbinates in the nasal cavity, which increases the cavity space for air. The air pathway has a complicated labyrinth-like structure; the inhaled and exhaled air takes tortuous paths. The actual air pathway follows a complex 3D trajectory in the connected paths of the coronal and sagittal planes induced by the changes in direction and local gap thickness. This contributes to most olfactory airflow departing from the main respiratory airflow path in the sagittal plane to the dorsal side in the coronal plane [24]. We particularly explored the geometric properties in the coronal plane to understand how odorant particles can be captured by the olfactory mucosa on the nasal wall.

Basic assessment is done by quantifying and comparing features of nasal cavity geometries, including the gap thickness, W, the radius of curvature, κ^{-1} , and the tortuosity, \mathcal{T} , which are illustrated in figure 1c,d. Here, the tortuosity is defined as the ratio of the arc length of a branch, $L_{\rm arc}$, to the shortest Euclidean distance between two points, L. We skeletonized the cross-sectional images and defined a branch as connected lines between neighbouring pixels to determine \mathcal{T} ; see electronic supplementary material, section A for details.

In general, the nasal cavities of large animals, except for humans, have large characteristic length scales, namely, the radius of curvature, κ^{-1} (mm), and gap thickness, W (mm), which follow an allometric relation $\kappa^{-1} \approx 1.14 \ W^{0.98}$ or $\kappa W^{0.98} \approx 0.88$ ($R^2 = 0.89$). However, the nasal structure of humans does not adhere to this trend; it has a comparatively much larger radius of curvature to its gap thickness. The distinct geometric features shared by the animals and not by humans may contribute mechanically to their superior sense of smell. The nasal cavity of pigs shows that the air passage swirls in a spiral fashion (figure 1a), which produces the highest tortuosity among the other animals. Comparatively, small animals such as marsupials and rodents, potoroo with longer curvy branches, exhibit the second-highest tortuosity. Other animals also have similar complex nasal structures, but shorter and more straight branches resulting in comparatively low tortuosity. The air is locally connected through various routes within nasal networks, resulting in a broad range of tortuosity measured around 1.31 for opposum, 1.30 for northern quoll, 1.45 for guinea pig, 1.72 for potoroo, 1.20 for rabbit, 1.20 for dog, 1.49 for human and 3.31 for pig. The method of measuring the tortuosity in this study is limited because it does not reflect the complex route of airflow. Instead, by measuring the tortuosity of the branches, the pathway of odorant particles can be inferred. Consequently, the tortuosity on the coronal plane approximately captures the complexity of the structure of the nasal bones of animals and provides a guide for the design of synthetic filters.

2.2. Basic filter geometry

Taking into account the value of the basic parameters obtained in the animal noses, we designed test filters consisting of arrays of conduits containing five levels of tortuosity, \mathcal{T} , following the allometric relationship shown in figure 1c. Figure 2 illustrates a straight ($\mathcal{T}=1.0$) and tortuous ($\mathcal{T}=1.4$, 1.8 and 2) channels with square cross-sections. The conduits are tortuous with sharp 90° turns and side

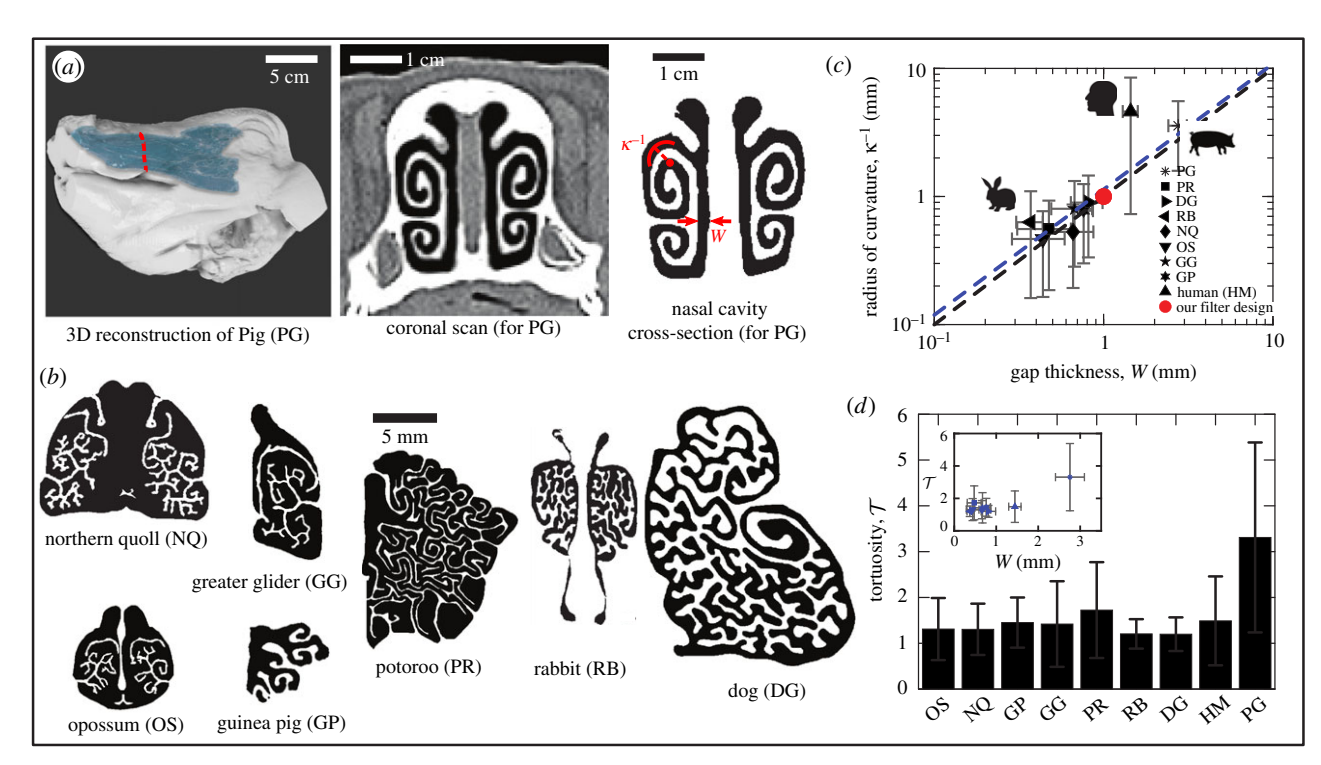


Figure 1. (a) Three-dimensional reconstructed model and coronal view from CT imaging of an adult pig. In the leftmost image, the light blue part represents the nasal structure. The image on the far right shows only the nasal airspace (in black), extracted from the CT scan. Detailed CT images are shown in electronic supplementary material, movies S1, S2, and S3. (b) Coronal views of the nasal structure of various animals (northern quoll, opossum, greater glider and potoroo images are adapted from Macrini et al. [20] with permission from T. E. Macrini. The guinea pig image is adapted from Rodgers [21] with permission from T. Rowe at DigiMorph.org. The rabbit image is adapted from Casteleyn et al. [22] with permission from Elsevier. The dog image is adapted from Craven et al. [23] with permission from B. Craven). (c) The relationship between the gap thickness and the radius of curvature measured in eight animals' skulls (blue-dotted line). The measured values have an R^2 of 0.89 to the diagonal line. The black-dotted line of unity slope is included for reference. (d) Measured tortuosity from the various animals' nasal cavity structures. Here, the x-axis is defined by the animal's weight.

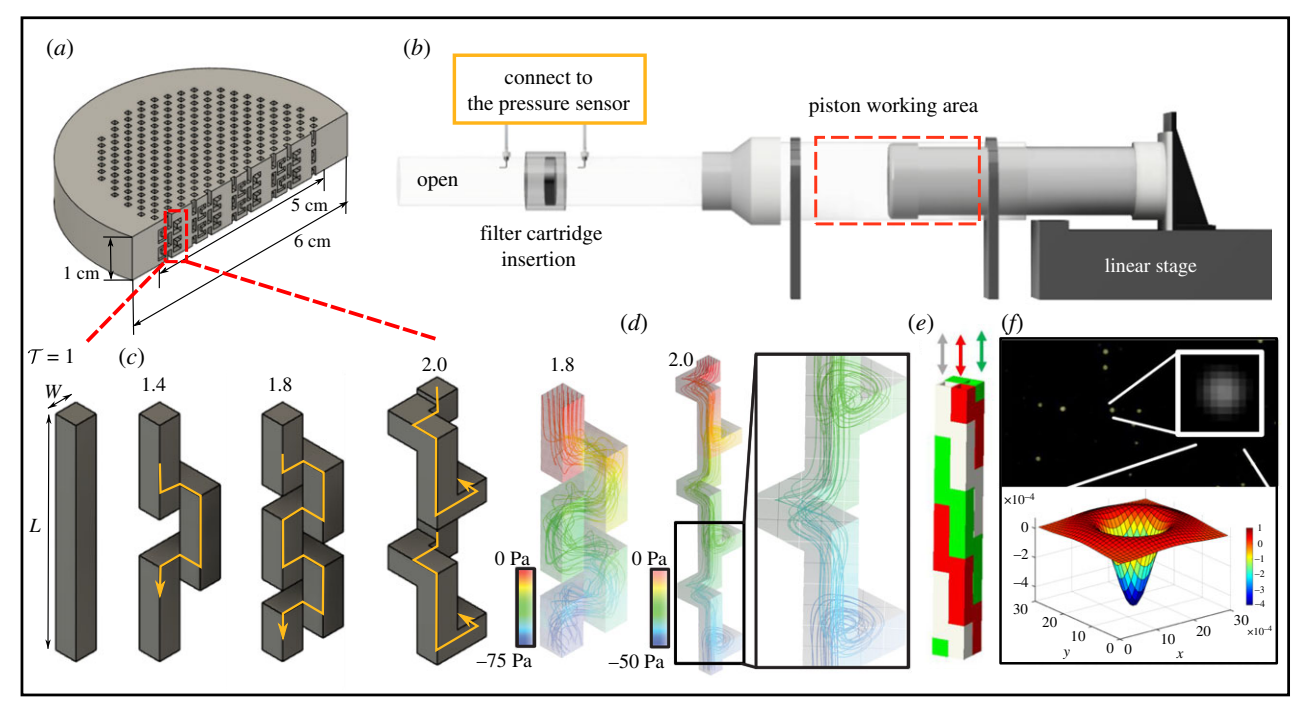


Figure 2. (a) Schematics of the filter with a 6 cm outer diameter and 5 cm inner diameter. The filter structure is tightly fit in the pipe system of (b). (b) Experimental set-up for pressure drop measurements; the left side has an open pipe structure with a filter in the middle. On the right side, the piston reciprocates due to a moving linear stage. (c) Schematics of filter conduits with different tortuosity, \mathcal{T} ; (d) examples of simulated streamlines in a single filter pathway highlighting complex mean flow trajectories; (e) example of 'packed' conduits for reduced pressure drop; (f) illustration of experimental particle characterization using Gaussian kernel.

walls of W=1 or W=0.4 mm. The range of tortuosity set, $\mathcal{T} \in [1, 2.0]$, covers most animal's nasal characteristics except for pigs.

2.3. Filter pressure drop

The tortuous filters are first tested for the pressure drop, ΔP , across 60 mm circular cross-section cartridges of 10 mm thickness containing 312 conduits arranged regularly within a 50 mm diameter region; see details and a view of the bulk geometry in figure 2a. Note that the geometry of the conduits allows for compact packing that minimizes material requirement and pressure drop (see an example in figure 2e). However, cartridges with an optimized layout are not needed here; a single conduit arrangement in an aligned pattern is better than typical filters such as N95, surgical mask and HEPA. As expected, the configurations with a higher level of tortuosity produce higher pressure drop for a given flow rate due to the local loss induced by the channel bends and longer pathway (figure 3a). Surgical mask, N95 and HEPA filters that share similar capturing efficiency range to our tortuous filters are used as reference cases to compare the relative pressure of the proposed filters.

The bulk pressure loss coefficient, *K*, of the various filters can be characterized as $\Delta P/\rho g = K U^2/2g$. Here, ρ is the air density, g is the gravitational constant and U is the averaged incoming airspeed. The pressure drop and characteristic coefficient *K* for each filter are shown in figure 3*b*. The new filters have a substantially lower pressure coefficient than the N95, surgical mask and HEPA filters. In particular, the highest pressure coefficient of the filter cartridge is still less than half of those of the surgical mask; $K(T = 1.8) \approx 0.5 K_{\text{surgical}}$. It is worth noting that the lower pressure drop is partially attributed to the hole size too, which we have not taken into account in this study. Such lower pressure drop indicates the direct benefit of these filters when used as respirators, and the reduced likelihood of air leakage from the boundaries of commercial masks. Complementary numerical simulations of filter cartridges performed for four flow rates using averaged Navier-Stokes equations are shown with open symbols in figure 3b.

2.4. Particle capture performance

The particle capture efficiency of the filters as a function of flow velocity and tortuosity is illustrated in figure 4. The higher filtering efficiency is achieved by both decreasing freestream velocity and increasing filter tortuosity. A comparatively greater increase in efficiency for smaller particles (i.e. diameter $d \le 12 \,\mu\text{m}$) is achieved with reduced inflow velocity; increasing tortuosity from 1.3 to 2, produces a small increment in efficiency for all particle sizes as shown in figure 4a. Figure 4c shows the filtering efficiency versus the particle Stokes number, Stk. Here, Stk = $d\rho_{\nu}$ $U/(18\mu)$ is the Stokes number and ρ_p is the density of particle and μ is the air dynamic viscosity. Two critical Stokes number values are observed for inflow velocities U = 0.2 and 0.4 m s⁻¹, where the typical positive correlation between deposition efficiency and Stokes number [27-29] is followed for different particle sizes; however, this does not hold for the change in inflow velocity. This can be explained by the lower tangential rebound angle for higher inflow velocity caused by a much lower coefficient of restitution [30], demonstrating that both rebound angle after a collision and Stokes

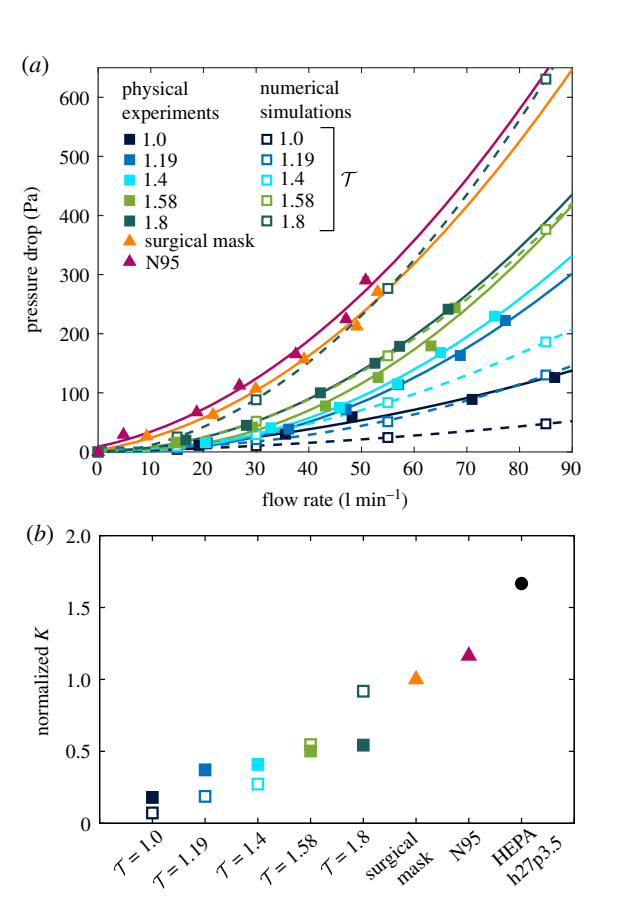


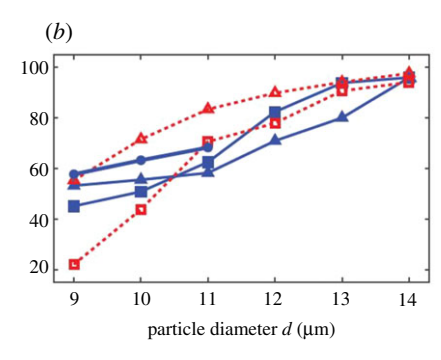
Figure 3. (a) Pressure drop across filters with different tortuosity values, \mathcal{T} . The corresponding measurements for the surgical mask, N95 and HEPA filters are included for reference [25]. (b) Pressure loss coefficient \mathcal{K} , normalized with respect to that of the surgical mask.

number effects are crucial during the particle trapping process within tortuous passages.

The particle capturing simulations in single tortuous pathways of tortuosity 1.3 and 2 agree with the trends from the experimental results. The higher velocity of airflow shows lower capturing efficiency at smaller diameters, whereas above 13 µm particles, both tortuosities reported a filter efficiency greater than 80%, which are comparable to those reported for cloth and surgical mask ranging from 85% to 99.9% [26,31]. Tortuosity increase (turns in the pathway geometry) showed enhanced capturing efficiency.

3. Discussion and remarks

Underlying bioinspiration of our filter design takes elements of the well-evolved morphological nasal structures seen in high-olfactory animals. Those allow for efficient capture of fine air particles onto the olfactory epithelium while maintaining a low-pressure drop and easy breathing. The newly engineered filter system aims to achieve similar goals: high particle capturing efficiency at a relatively low-pressure drop. The CT scan images of nine mammal nasal structures showed very tortuous intranasal air paths, which are quantified by the tortuosity parameter \mathcal{T} that varied between 1.2 and 3.3, and the radius of curvature that was proportional to the gap thickness. Based on these basic morphological relationships in animals, we designed filters with simplified geometries and manufactured them using home-use and professional 3D-printers. Laboratory tests showed that the pressure drop across the filter increases with tortuosity



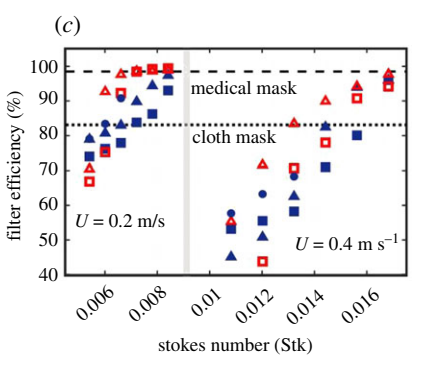


Figure 4. Particle filtering for a mean velocity of (a) 0.2 m s^{-1} and (b) 0.4 m s^{-1} ; experiments include double cartridges. (c) Deposition efficiency versus Stokes number compared with the median filter efficiency of the medical (dashed line) and cloth (dotted line) masks [26].

owing to the additional curves; however, the pressure difference requirement was almost two times smaller than that of commercial filters (surgical, N95 and HEPA), despite the arrangements of the tortuous conduits being not efficiently packed. If needed, the filtration capability can be adjusted easily by changing the tortuosity levels and adding filter layers. Pressure drop may be also substantially reduced with efficient conduit packing. Indeed, an increase of over three times in the effective conduit area can result from the compact packing (shown in figure 2e) applied in the cartridge used for testing.

The proposed filter design replicates the tortuosities of the animal airway passages as measured on the coronal sections, which has been illustrated in electronic supplementary material, figure S1. We did not measure the tortuosities on the axial and sagittal planes, as they have somewhat limited role in facilitating particle capture from the inhaled air. Turbinate structures in high-olfactory animals (e.g. dogs, opossum, etc.) are distinctly more convoluted than in human nasal cavities. Such complexity of the nasal morphology on the coronal cross-sections promotes mixing [32] of the inhaled air leading to increased capture of the small odorants along the olfactory epithelium (located along the roof of the upper airway). Note that the novelty of our filter design is implicit in the use of the highly tortuous air transmission passages that ensure particle trapping along the internal walls of each passage, thereby accommodating relatively large inlet holes at the filter surface that facilitate breathability and less energy expenditure. Comparable filtration technologies (e.g. cloth masks, surgical masks, N95 covers) rely [33] on small hole sizes with random spatial arrangements of fibres.

Downloaded from https://royalsocietypublishing.org/ on 26 May 2022

As illustrated in figure 4, the filter prototypes for two tortuosities (viz. T = 1.3, 2.0) were tested to evaluate their particle capturing efficiency for particle sizes $d \in [9, 14] \, \mu m$. In a recent study [14], we computationally tracked inhaled air embedded with representative particulate size distribution [34]. The initial airway infection hot spots for airborne respiratory viruses are at the nasopharynx, with ciliated epithelial cells bearing ACE2 surface receptors, located at the back of nose and throat. Inhaled particles that land directly at the hot spots, thereby triggering the infection, belong to the size range of $\approx 2-20 \,\mu\text{m}$. In such context, a reprocessing (see electronic supplementary material, figure S4) of the published in silico data indicates an interesting trend: 84.4% of the viral load transmission is orchestrated by particles with diameter $\tilde{d} \ge 9 \,\mu\text{m}$. To implement effective air sanitation, our filter prototypes hence carry out a targeted screening of only the more pathogenic particles at lower energy expenditure (figure 3) when compared to other state-of-the-art filters across scales.

Our novel filter design can be helpful in many industrial and biomedical applications in which high collection efficiency and low-pressure drop are crucial. For example, many have experienced a shortage of personal protective devices and medical ventilators during the peak of the pandemic in 2020. At a small scale, our 3D-printed model can replace other mask filters to reduce the pressure drop while supporting high particle capturing rates. For example, 31 g of filament in a 3D-printer are enough to print one of our filter cartridges, which costs only about \$2.1 based on the Ultimaker PLA market price as of 2021. Our filters are not disposable, and can be usable multiple times after sterilization. Hence, in the long run they are cheaper and help reduce waste. It should be also be noted that this bioinspired filter concept is also significantly scalable for various applications that may demand industry-level air filtering.

4. Methods

4.1. Animal nasal analysis using computed tomography scan images

CT scan images for the pig were taken using Toshiba Aquilion 16-slice CT scanner, which provides 0.5 mm slice resolution. The Dasyurus hallucatus (northern quoll), Caluromys philander (bare-tailed woolly opossum), Petauroides volans (greater glider) and Potorous tridactylus (long-nosed potoroo) CT scan images were acquired by Dr Macrini [20]. For the rabbit, the dorsal view of histological section was acquired from Casteleyn et al. [22]. The high-resolution magnetic resonance image of the dog was obtained from Craven et al. [23]. The guinea pig's CT scan images were obtained from Ms Jeri Rodgers [21]. The nasal cavity portion from the coronal view of nasal images obtained from MATLAB impage processing toolbox was processed as a black and white binary image to measure the gap thickness, curvature and tortuosity using IMAGEJ software. The measurement method of each characteristic is described in the electronic supplementary material, section A.

4.2. Design and three-dimensional printing of mask filters

We used key common features of the nasal structure of mammalian turbinates. This structure compartmentalizes the incoming airflow into several tortuous channels in a distinct way that maximizes particle capture. Following a similar relation between

the tortuosity and channel width, we design 3D mask structures. The designed filters ($\mathcal{T} \in [1,\ 1.8]$) were sliced through Cura software (Ultimaker Ltd). The print settings for slicing are set as 0.2 mm for the layer height, 0.4 mm for the line width, 100% for the infill percentage and 0.8 mm for the wall thickness. The filters were 3D printed by using Ultimaker S5 (Ultimaker Ltd) with Ultimaker 2.85 mm NFC PLA (Ultimaker Ltd). For the highest tortuous filter $\mathcal{T}=2.0$, Shapeways Corp. used the ProJet® MJP 3500 (3D System Ltd) printer with the VisiJet® M3 Crystal material.

4.3. Experimental set-up for pressure drop

measurements

A piston was used to control the airflow through the filter, while measuring the pressure drop across the filter (figure 2b). The piston setting consisted of three parts. A 2-inch clear rigid pipe (49035K48, McMaster-Carr Supply Co.) was used for the inlet part. A two-pipe female socket connector (9161K46, McMaster-Carr Supply Co.) was used for the middle part where the filter cartridge was located. The last outlet part was composed of a 2-inch clear rigid pipe (49035K48, McMaster-Carr Supply Co.) and piston. To construct the piston, a 3-inch clear rigid pipe (49035K49, McMaster-Carr Supply Co.) was used for the inner piston, and a 4-inch clear rigid pipe (49035K51, McMaster-Carr Supply Co.) was used for the outer surrounding inner piston. In addition, a straight reducer (4880K018, McMaster-Carr Supply Co.) was used to connect 2-inch and 4-inch clear rigid pipes.

Small holes upwind and downwind the filter cartridge were used to measure pressure drop. A 90° anemometer was connected to the pressure sensor and Data Acquisition Card (DAQ Card, DAQ Systems by NITM). The analogue input voltage data were measured through the DAQ Card was converted to pressure through a calibration curve following standard procedure (see electronic supplementary material, section B). Also, the speed of airflow versus piston speed was measured by using laser sheets, fog particles and a high-speed camera. The fog particle was injected into the left side of the filter, then it was inhaled to the right side by the piston moving. High-speed videos were used for velocimetry using Tracker software as a complement.

4.4. Experimental set-up for particle capturing efficiency

The particle capturing efficiency of the designed filters was experimentally measured in a 500 mm long, 40 mm wide, and 40 mm high wind tunnel located in the Renewable Energy and Turbulent Environment Laboratory at the University of Illinois. A Sunon Fans 12V DC brushless fan was installed upwind of the inlet followed by a contraction section with an area ratio of 25:1. A flow straightener was installed near fans and another was installed at the beginning of the channel to ensure flow uniformity. The fan generates volumetric airflows up to 24 cubic feet per minute (CFM). A single ADG-SK508 compression-type nozzle was used to generate particles of diameters ranging from 9 µm to 15 µm, which approximately mimics the particle condition of human breathing [35]. Aqueous chlorophyll solution of approximately 2.4% by volume was used as the fluid feeding into the nebulizer to increase particle light reflectivity to a 532 µm wavelength laser. This allowed for particle sizing and distribution.

Two field of views (FOVs) of interest are selected with their centre located 40 and 80 mm upwind and downwind the filter. The incoming and filtered particle size and shape distributions were acquired across a streamwise plane using a low-speed,

high-resolution planar PIV system from TSI. Two cameras both equipped with 25 mm, F 2.8 LOWA ultra macro-lens with $\times 5$ magnification, were used to interrogate two 3.87×2.90 mm FOVs. The FOVs were located at the centre of the wind tunnel in both spanwise and wall normal direction. The FOVs were illuminated from a 250 mJ pulse⁻¹ Quantel double-pulsed laser. Five sets of 100 image pairs were collected at an acquisition frequency of 2.4 Hz, using a pair of 8 MP (3320 \times 1560 pixels) CCD cameras with 16 bit frame-straddle; see additional information in electronic supplementary material, figure S3.

4.5. Particle size analysis

Iterative Laplacian of Gaussian (LoG) filtering was used for particle sizing. The generalized LoG filter, as introduced by Kong *et al.* [36], was used to detect the blobs in the images. The two-dimensional LoG kernel was generated by applying the Laplacian operator ∇^2 in the Gaussian function $G(x, y; \sigma)$, resulting the following kernel:

$$\nabla^{2}G(x, y; \sigma) = \frac{x^{2} + y^{2} - 2\sigma^{2}}{\pi\sigma^{4}} \exp\left(-\frac{x^{2} + y^{2}}{2\sigma^{2}}\right). \tag{4.1}$$

The LoG kernel was then convoluted with the blob-like structures to return a fitting score. This process was performed in an iterative manner with increasing σ LoG kernels, where the best fit scale of σ_0 was determined when the fitting score converges to a local maximum, the radius of particle was then obtained as $r=\sqrt{2}\sigma_0$ [37]. This algorithm was applied to each blob-like structure in the image with an adaptive threshold to filter out the unfocused outliers allowing accurate particle size distribution from the PIV images; see the example in electronic supplementary material, figure S4d.

4.6. Computational model

The *in silico* geometrical set-up to track the pressure drop across a filter consisted of short upwind and downwind conduits with the circular filter (extracted from the filter stereolithography files) being placed in between. To explore the transport mechanism in more detail, we also reconstructed a single air passage pathway ($\approx \! 300$ of which placed in a circular grid assembly would comprise one complete filter prototype) for each of the tortuous designs and simulated the inhaled airflow and particle transport therein.

4.7. Airflow simulation

The numerical simulations in the meshed filter domains considered four airflow rates, viz. 15, 30, 55 and 85 l min⁻¹. The low flow rate, even in tortuous pathways, is dominated by viscous-laminar steady-state flow physics [38-43]; the higher flow rates trigger separation from the tortuous walls, resulting in flow fluctuations. We have replicated such regimes through large eddy simulation (LES), accounting for the small fluctuations with a sub-grid scale kinetic energy transport model [44]. The computational scheme employed a segregated solver, with pressure-velocity coupling and the second-order upwind spatial discretization. We monitored solution convergence by minimizing the mass continuity and velocity component residuals, and through stabilizing the mass flow rate and static pressure at the airflow outlets. The density and dynamic viscosity of inhaled air were set to 1.204 kg m⁻³ and $1.825 \times 10^{-5} \text{ kg m}^{-1} \text{ s.}$

4.8. Particle capturing efficiency

Particle dynamics against the ambient airflow passing through the filter were tracked by Lagrangian-based discrete phase inert transport simulations with the localized deposition and

royalsocietypublishing.org/journal/rsif J. R. Soc. Interface 19: 20210849

clustering along the filter walls obtained through numerically integrating the transport equation:

$$\frac{\mathrm{d}\mathbf{u}_p}{\mathrm{d}t} = \frac{18\mu}{d^2\rho_p} \frac{C_D Re}{24} (\mathbf{u} - \mathbf{u}_p) + \mathbf{g} \left(1 - \frac{\rho}{\rho_p} \right) + \mathbf{F_B}. \tag{4.2}$$

Here \mathbf{u}_p represents the particle velocity, \mathbf{u} is the airflow field velocity, ρ and ρ_p , respectively, are the density of inhaled air and the particle material density, \mathbf{g} is the gravitational acceleration, and $\mathbf{F}_{\mathbf{B}}$ accounts for any other additional body forces per unit particle mass (e.g. Saffman lift force which is exerted by a typical flow-shear field on small particulates transverse to the airflow direction). The term $18\mu C_D$. $Re~(\mathbf{u}-\mathbf{u}_p)/24(d^2\rho_p)$ quantifies the drag force contribution per unit particle mass, with C_D representing the drag coefficient, d representing the particle diameter, and Re is the relative Reynolds number. Also, the particle size range is considered large enough to neglect Brownian motion effects on their dynamics.

To replicate the physical conditions of dehydrated airborne particles in the numerical simulations, the particle material density was kept at 1100 kg m⁻³. Trap boundary condition, whereby a particle motion would cease when it reaches the cells adjacent to the geometry surface, is not applied on all inner walls, but on selected walls with comparatively low wall shear stress. Particles are assumed to shear away and separate from the walls with higher wall shear values. Details of the numeric protocol (based off published findings, e.g. [30,45]) can be found in electronic supplementary material, section D.

Data accessibility. All scripts used in this study are openly accessible through https://github.com/StochasticBiology/boolean-efflux.git. The data supporting the findings of this study are available in electronic supplementary material.1 [46]. Other datasets analysed during the current study are available from the corresponding author upon request.

Authors' contributions. J.Y.: data curation, formal analysis, investigation, methodology, visualization, writing—original draft, writing—review and editing; A.C.: formal analysis, investigation, software, writing—original draft; S.C.: data curation, formal analysis, investigation, methodology, visualization, writing—original draft, writing—review and editing; C.C.: data curation, formal analysis, investigation, methodology, visualization, writing—original draft; A.J.: investigation, methodology, software, visualization, writing—original draft; S.B.: conceptualization, funding acquisition, project administration, software, writing—original draft, writing—review and editing; S.J.: conceptualization, funding acquisition, project administration, writing—original draft, writing—review and editing, writing—original draft, writing—review and editing.

All authors gave final approval for publication and agreed to be held accountable for the work performed therein.

Competing interests. We declare we have no competing interests. Funding. J.Y. and S.J. acknowledge funding support from the National Science Foundation (NSF) grant no. CBET-2028075. L.P.C. acknowledges funding support from the NSF grant no. CBET-2028090. S.B. acknowledges funding support from the NSF grant no. CBET-2028069.

References

- Souzandeh H, Wang Y, Netravali AN, Zhong W-H. 2019 Towards sustainable and multifunctional airfilters: a review on biopolymer-based filtration materials. *Polymer Rev.* 59, 651–686. (doi:10.1080/ 15583724.2019.1599391)
- Liu B, Zhang S, Wang X, Yu J, Ding B. 2015 Efficient and reusable polyamide-56 nanofiber/nets membrane with bimodal structures for air filtration. *J. Colloid Interface Sci.* 457, 203–211. (doi:10.1016/ i.jcis.2015.07.019)
- Li M, Feng Y, Wang K, Yong WF, Yu L, Chung T-S. 2017 Novel hollow fiber air filters for the removal of ultrafine particles in PM_{2.5} with repetitive usage capability. *Environ. Sci. Technol.* 51, 10 041–10 049. (doi:10.1021/acs. est.7b01494)
- Jung S, Kim J. 2020 Advanced design of fiber-based particulate filters: materials, morphology, and construction of fibrous assembly. *Polymers* 12, 1714. (doi:10.3390/polym12081714)
- Zhu M et al. 2017 Electrospun nanofibers membranes for effective air filtration. Macromol. Mater. Eng. 302, 1600353. (doi:10.1002/mame.v302.1)
- Brown RC. 1993 Air filtration: an integrated approach to the theory and applications of fibrous filters. Oxford, UK: Pergamon Press.
- Kang S, Lee H, Kim SC, Chen D-R, Pui DY. 2019 Modeling of fibrous filter media for ultrafine particle filtration. Sep. Purif. Technol. 209, 461–469. (doi:10. 1016/j.seppur.2018.07.068)
- Castro J, Ostoja-Starzewski M. 2000 Particle sieving by percolation through a random fiber network. *Appl. Math. Model.* 24, 523–534. (doi:10.1016/ S0307-904X(99)00055-4)

- Bliss T, Castro J, Ostoja-Starzewski M. 2015 A threedimensional model of fine particle retention during percolation through a fiber mat. *TAPPI J.* 14, 546—554. (doi:10.32964/TJournal)
- Feng S, Gao D, Liao F, Zhou F, Wang X. 2016 The health effects of ambient *PM*_{2.5} and potential mechanisms. *Ecotoxicol. Environ. Saf.* 128, 67–74. (doi:10.1016/j.ecoenv.2016.01.030)
- Bazant MZ, Bush JW. 2021 A guideline to limit indoor airborne transmission of COVID-19. *Proc. Natl Acad. Sci. USA* 118, e2018995118. (doi:10.1073/pnas.2018995118)
- 12. Mittal R, Ni R, Seo J-H. 2020 The flow physics of COVID-19. *J. Fluid Mech.* **894**, F2. (doi:10.1017/jfm.2020.330)
- Stadnytskyi V, Bax CE, Bax A, Anfinrud P. 2020 The airborne lifetime of small speech droplets and their potential importance in SARS-CoV-2 transmission. *Proc. Natl Acad. Sci. USA* 117, 11 875–11 877. (doi:10.1073/pnas.2006874117)
- 14. Basu S. 2021 Computational characterization of inhaled droplet transport to the nasopharynx. *Sci. Rep.* **11**, 1–13. (doi:10.1038/s41598-020-79139-8)
- Chaudhuri J, Baukelmann A, Boettcher K, Ehrhard P.
 2019 Pressure drop in fibrous filters. *Eur. J. Mech.-B/Fluids* 76, 115–121. (doi:10.1016/j.euromechflu. 2019.01.013)
- Laska M. 2017 Human and animal olfactory capabilities compared. In *Springer handbook of odor*, (ed. A Buettner), pp. 678–681. Cham, Switzerland: Springer. (doi:10.1088/1757-899X/36/1/012038)
- Spencer TL, Clark A, Fonollosa J, Virot E, Hu DL.
 2021 Sniffing speeds up chemical detection by controlling air-flows near sensors. *Nat. Commun.* 12, 1–10. (doi:10.1038/s41467-020-20314-w)

- Zwicker D, Ostilla-Mónico R, Lieberman DE, Brenner MP. 2018 Physical and geometric constraints shape the labyrinth-like nasal cavity. *Proc. Natl Acad. Sci. USA* 115, 2936–2941. (doi:10.1073/pnas. 1714795115)
- Gac JM, Jackiewicz A, Werner Ł., Jakubiak S. 2016 Consecutive filtration of solid particles and droplets in fibrous filters. Sep. Purif. Technol. 170, 234–240. (doi:10.1016/j.seppur.2016.06.057)
- Macrini TE. 2012 Comparative morphology of the internal nasal skeleton of adult marsupials based on X-ray computed tomography. *Bull. Am. Mus. Nat. Hist.* 2012, 1–91. (doi:10.1206/365.1)
- Rodgers MJ. 2012 Cavia porcellus. Guinea pig, digital morphology. See http://digimorph.org/specimens/ Cavia_porcellus/ (accessed 3 January 2021).
- Casteleyn C, Broos A, Simoens P, Van Den Broeck W. 2010 NALT (nasal cavity-associated lymphoid tissue) in the rabbit. Vet. Immunol. Immunopathol. 133, 212–218. (doi:10.1016/j.vetimm.2009.08.011)
- Craven BA, Paterson EG, Settles GS, Lawson MJ. 2009 Development and verification of a high-fidelity computational fluid dynamics model of canine nasal airflow. J. Biomech. Eng. 131, 091002. (doi:10.1115/ 1.3148202)
- Craven BA, Paterson EG, Settles GS. 2010 The fluid dynamics of canine olfaction: unique nasal airflow patterns as an explanation of macrosmia. J. R. Soc. Interface 7, 933–943. (doi:10.1098/rsif.2009.0490)
- Del Fabbro L, Laborde J, Merlin P, Ricciardi L. 2002
 Air flows and pressure drop modelling for different
 pleated industrial filters. *Filt. Sep.* 39, 34–40.
 (doi:10.1016/S0015-1882(02)80055-6)

- Aydin O, Emon B, Cheng S, Hong L, Chamorro LP, Saif MTA. 2020 Performance of fabrics for homemade masks against the spread of COVID-19 through droplets: a quantitative mechanistic study. *Extr. Mech. Lett.* 40, 100924. (doi:10.1016/j.eml. 2020.100924)
- Verjus R, Angilella J-R. 2016 Critical stokes number for the capture of inertial particles by recirculation cells in two-dimensional quasisteady flows. *Phys. Rev. E* 93, 053116. (doi:10.1103/PhysRevE.93.053116)
- 28. Nicolaou L, Zaki TA. 2015 On the stokes number and characterization of aerosol deposition in the respiratory airways. In *CMBE15 4th Int. Conf. on Computational and Mathematical Biomedical Engineering, 29 June–1 July, Cachan, France* (eds P Nithiarasu, E Budyn), pp. 224-227. See https://www.compbiomed.net/getfile.php?type=12/site_documents&id=Proceedings_2227-9385_compressed.pdf.
- Rader DJ, Geller AS. 2008 Transport and deposition of aerosol particles. In *Developments in surface* contamination and cleaning (eds R Kohli, K Mittal), pp. 189–266. Norwich, NY: William Andrew Publishing. (doi:10.1016/B978-081551555-5. 50005-8)
- Fan F-G, Ahmadi G. 1995 Analysis of particle motion in the near-wall shear layer vortices—application to the turbulent deposition process. *J. Colloid Interface* Sci. 172, 263–277. (doi:10.1006/jcis.1995.1252)
- Konda A, Prakash A, Moss GA, Schmoldt M, Grant GD, Guha S. 2020 Aerosol filtration efficiency of common fabrics used in respiratory cloth masks. ACS Nano 14, 6339–6347. (doi:10.1021/acsnano. 0c03252)

- Tracy LF, Basu S, Shah PV, Frank-Ito DO, Das S, Zanation AM, Kimbell JS. 2019 Impact of endoscopic craniofacial resection on simulated nasal airflow and heat transport. *Int Forum Allergy Rhinol.* 9, 900–909. (doi:10.1002/alr.22328)
- Clapp PW, Sickbert-Bennett EE, Samet JM, Berntsen J, Zeman KL, Anderson DJ, Weber DJ, Bennett WD. 2021 Evaluation of cloth masks and modified procedure masks as personal protective equipment for the public during the COVID-19 pandemic. *JAMA Intern. Med.* 181, 463–469. (doi:10.1001/jamainternmed.2020.8168)
- 34. Xie X, Li Y, Sun H, Liu L. 2009 Exhaled droplets due to talking and coughing. *J. R. Soc. Interface* **6**, S703–S714. (doi:10.1098/rsif.2009.0388.focus)
- 35. Bake B, Larsson P, Ljungkvist G, Ljungström E, Olin A. 2019 Exhaled particles and small airways. *Respir. Res.* **20**, 1–14. (doi:10.1186/s12931-019-0970-9)
- Kong H, Akakin HC, Sarma SE. 2013 A generalized Laplacian of gaussian filter for blob detection and its applications. *IEEE Trans. Cybern.* 43, 1719–1733. (doi:10.1109/TSMCB.2012.2228639)
- Wang G, Lopez-Molina C, De Baets B. 2020
 Automated blob detection using iterative Laplacian of Gaussian filtering and unilateral second-order Gaussian kernels. *Digit. Signal Process.* 96, 102592. (doi:10.1016/j.dsp.2019.102592)
- Basu S *et al.* 2020 Numerical evaluation of spray position for improved nasal drug delivery. *Sci. Rep.* 10, 1–18. (doi:10.1038/s41598-019-56847-4)
- Inthavong K, Ma J, Shang Y, Dong J, Chetty ASR, Tu J, Frank-Ito DO. 2019 Geometry and airflow dynamics analysis in the nasal cavity during

- inhalation. *Clin. Biomech.* **66**, 97–106. (doi:10.1016/j.clinbiomech.2017.10.006)
- Zhang Y, Shang Y, Inthavong K, Tong Z, Sun B, Zhu K, Yu A, Zheng G. 2019 Computational investigation of dust mite allergens in a realistic human nasal cavity. *Inhal. Toxicol.* 31, 224–235. (doi:10.1080/08958378.2019.1647315)
- Basu S, Frank-Ito DO, Kimbell JS. 2018
 On computational fluid dynamics models for sinonasal drug transport: relevance of nozzle subtraction and nasal vestibular dilation. *Int. J. Numer. Methods Biomed. Eng.* 34, e2946. (doi:10.1002/cnm.2946)
- Farzal Z et al. 2019 Comparative study of simulated nebulized and spray particle deposition in chronic rhinosinusitis patients. Int Forum Allergy Rhinol. 9, 746–758. (doi: 10.1002/alr.22324).
- 43. Kimbell JS *et al.* 2019 Upper airway reconstruction using long-range optical coherence tomography: effects of airway curvature on airflow resistance. *Lasers Surg. Med.* **51**, 150–160. (doi:10.1002/lsm. v51.2)
- Baghernezhad N, Abouali O. 2010 Different SGS models in large eddy simulation of 90° square cross-section bends. *J. Turbul.* 11, N50. (doi:10. 1080/14685248.2010.520016)
- Haron A, Ismail K. 2012 Coefficient of restitution of sports balls: a normal drop test. *IOP Conf. Ser.: Mater. Sci. Eng.* 36, 012038. (doi:10.1088/1757-899X/36/1/012038)
- Yuk J, Chakraborty A, Cheng S, Chung C-I,
 Jorgensen A, Basu S, Chamorro LP, Jung S 2022 On
 the design of particle filters inspired by animal
 noses. Figshare.